Optical pulse dynamics for quantum-dot logic operations in a photonic-crystal waveguide

Xun Ma and Sajeev John
Department of Physics, University of Toronto, Toronto, Ontario, M5S 1A7 Canada
(Received 15 September 2011; published 28 November 2011)

We numerically demonstrate all-optical logic operations with quantum dots (QDs) embedded in a bimodal photonic-crystal waveguide using Maxwell-Bloch equations in a slowly varying envelope approximation (SVEA). The two-level QD excitation level is controlled by one or more femtojoule optical driving pulses passing through the waveguide. Specific logic operations depend on the relative pulse strengths and their detunings from an inhomogeneouslly broadened (about 1% for QD transitions centered at 1.5 μm) QD transition. This excitation controlled two-level medium then determines passage of subsequent probe optical pulses. Envelope equations for electromagnetic waves in the linear dispersion and cutoff waveguide modes are derived to simplify solution of the coupled Maxwell-Bloch equations in the waveguide. These determine the quantum mechanical evolution of the QD excitation and its polarization, driven by classical electromagnetic (EM) pulses near a sharp discontinuity in the EM density of states of the bimodal waveguide. Different configurations of the driving pulses lead to distinctive relations between driving pulse strength and probe pulse passage, representing all-optical logic AND, OR, and NOT operations. Simulation results demonstrate that such operations can be done on picosecond time scales and within a waveguide length of about 10 μm in a photonic-band-gap (PBG) optical microchip.

DOI: 10.1103/PhysRevA.84.053848 PACS number(s): 42.70.Qs, 42.50.Hz, 32.80.−t, 42.50.Ct

I. INTRODUCTION

Photonic-band-gap (PBG) materials are a special class of photonic crystals (PCs) that facilitate light localization [1,2] and control of spontaneous emission [3,4] from atoms. The ability to control light on a microscopic level with engineered PC defect structures make PBG materials a versatile platform for micro- and nanophotonic devices. PBG-based devices can have significantly better performance than their conventional counterparts, due to strong light confinement on the subwavelength scale. The small PC defect mode volume leads to extremely strong optical fields at very low power levels for exceptional nonlinear optical effects. Moreover, PBG waveguides enable subwavelength scale circuits for diffractionless guidance of light on a chip in three dimensions [5–9].

In addition to strong field confinement effects, PBG materials benefit from their unprecedented capability of modifying the vacuum electromagnetic (EM) density of states (DOS) over extended volumes and spectral ranges. It has been recently shown that discontinuous local DOS inside photonic crystals can bring novel strong coupling dynamics, especially when the interaction time scale Δ_t (e.g., pulse duration, observation time, etc.) is comparable to or much longer than the relaxation time scale $1/\Gamma$. For example, in the steady state regime where $\Delta_t \gg 1/\Gamma$, a discontinuous jump from low to high local DOS at a cutoff frequency in a bimodal waveguide enables switching of two-level quantum dot (QD) populations from below to above inversion using a continuous wave (CW) driving laser field [10–12]. This is due to the imbalance of radiative emission rates among the laser-induced Mollow sidebands that are made to straddle the LDOS discontinuity.

The steady state population switching turns into a more dramatic dynamic population switching [13,14] for a coherent optical pulse with duration comparable with radiative relaxation rates ($\Delta_t \sim 1/\Gamma$). Near the LDOS discontinuity, radiative relaxation rates of the driven QD become highly field dependent. This enables control of radiative relaxation rates through field strength, and dynamical alteration of the interaction regime (from coherent transient to field-enhanced decay and vice versa) within a single pulse duration. In this mixed interaction time scenario, population inversion can be activated and deactivated by picosecond pulse trains detuned below and above the atomic resonance, respectively.

This dynamic switching effect forms the basis for all-optical switching proposed earlier [13,14]. Picosecond (control) pulse trains are sent through the linear dispersion mode of a PC bimodal waveguide embedded with two-level QDs. The other waveguide mode has a cutoff below the QD transition and control pulse frequencies, creating a discontinuous DOS jump. The QD populations can be switched to above and below inversion level by control pulses detuned below and above QD transition level, respectively. The pulse-controlled QD population then determines whether subsequent signal pulses can pass through the waveguide (with QDs above inversion) or not (with QDs below inversion). Furthermore, as demonstrated previously [15], an additional, weaker driving pulse (signal pulse) introduces rich modulation effects in the final QD inversion when its frequency coincides with the QD Mollow sidebands induced by the control (holding) pulse. This bichromatic modulation effect enables a complete set of all-optical logic operations [15]. Figure 1 provides a schematic illustration of a possible PBG waveguide structure and the corresponding photonic band spectrum for the proposed all-optical switching and logic operations.

Switching and logic devices were modeled earlier [13–15] as a *point in space*, involving only the optical Bloch equation but with pulses imposed as prescribed external fields at the QD location. In this case, only temporal evolution of the QD population was simulated. Alternatively, a simple model of optical switching can be obtained [17,18] by treating the response of QDs distributed in a PC waveguide as a steady state nonlinear susceptibility. However, the complete temporal and spatial evolution of the system requires solution of Maxwell's equation governing the pulse propagation together with the

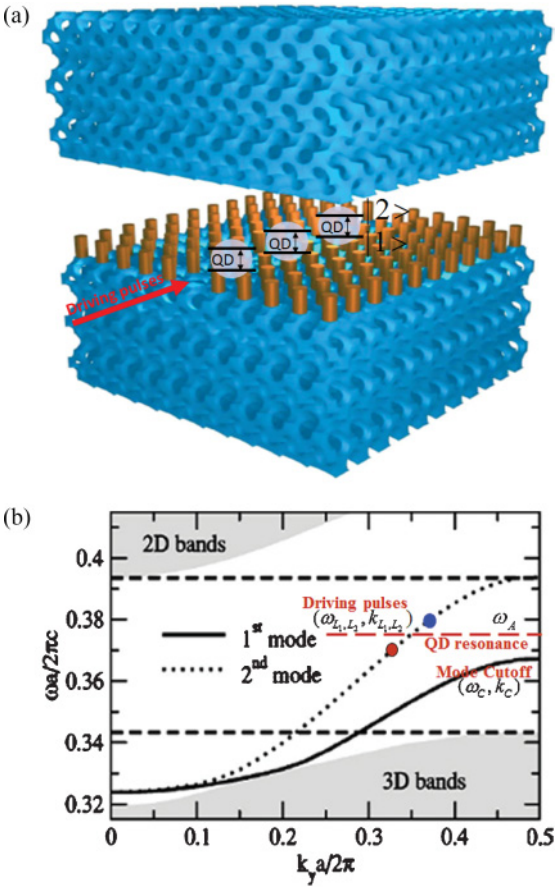

FIG. 1. (Color online) (a) Schematic structure and (b) spectrum of 2D-3D PBG waveguides [5,16] embedded with QDs for application in all-optical switching and logic.

optical Bloch equation for the QD. A self-consistent solution of the Maxwell-Bloch equations using a full finite-difference-time-domain (FDTD) simulation has been presented [19] in idealized one-dimensional (1D) and two-dimensional (2D) photonic-crystal structures. In this model, spontaneous emission dynamics is determined numerically from solution of Maxwell's equations in the vicinity of the light emitter. This dynamics depends specifically on the frequency of emission and the detailed dielectric geometry of the photonic crystal. There is no requirement to introduce radiative decay parameters by hand as in earlier studies [13–15]. This self-consistent theory captures stimulated emission and coherent feedback effects of the atomic Mollow sidebands, leading to remarkable high-contrast QD population switching. This occurs with only modest jump discontinuities in the electromagnetic LDOS, compared to simulations of the Bloch equation alone [13,14]. However, in Ref. [19] all QDs are concentrated in one spatial plane that cuts the waveguide. This study focused mainly on the temporal evolution of the QD population rather than pulse reshaping.

In the present paper we study the evolution of picosecond laser pulses along the waveguide and the resulting spatial population profile of QDs evenly distributed along the waveguide. Intense computational power is required for a full numerical solution of the Maxwell-Bloch equation in a two- or three-dimensional PBG waveguide [19]. In our paper we simplify modeling of the electromagnetic wave propagation by abstracting the key properties of the PBG waveguide modes and their interaction with QDs using a slowly varying envelope approximation (SVEA) [20–22]. Envelope equations of the electromagnetic waves in the linear dispersion and cutoff modes are derived with the PBG waveguide treated as an effective one-dimensional system. The envelope equations contain fitting parameters to match the dispersion curves of a realistic PBG waveguide structure. The input laser field induces QD dipole oscillations, which lead to radiative emission into both the linear dispersion mode and the cutoff mode. The radiation into the linear dispersion mode leads to backreaction on the input laser fields and modifies the pulse temporal profiles. Simultaneously, radiation into the cutoff mode provides feedback that drives the QDs. The envelop function of radiation in the cutoff mode satisfies a nonlinear Schrödinger equation derived using a quadratic approximation of the dispersion curve near the cutoff point [21,22]. The strong interaction between the QDs and the linear and cutoff modes occurs close to the DOS discontinuity caused by the cutoff. The evolution of QD populations and dipoles under this interaction is described by an atomic Bloch vector driven by fields at two distinct frequencies in structured vacuum [15]. It is based on this set of coupled Maxwell-Bloch equations that the temporal and spatial evolution of QD populations and driving pulses are simulated. For realistic results, inhomogeneous broadening effects of the QD transition frequencies (about 1% for QD transitions centered at 1.5 μm) is also included in our simulations. Unlike the fully self-consistent Maxwell-Bloch theory [19] in which radiative decay is determined by Maxwell's equations, we simplify the problem by inserting radiative decay rates by hand into the Bloch equations of the quantum dots. As a result, our model neglects non-Markovian feedback effects [19] in the radiation process.

In Sec. II we derive the envelop equations of the linear dispersion and cutoff modes, coupled with the structured vacuum QD Bloch equations. In Sec. III, as a consistency check, we recapture the well known phenomenon of self-induced transparency. This is followed by simulation results of an all-optical switching device and all-optical AND, OR, and NOT logic devices embedded in a 10 μm length segment of the PBG waveguide. The possibility of soliton formation inside the waveguide over longer distances is also explored.

II. COUPLED MAXWELL-BLOCH EQUATIONS

We first consider the propagation of picosecond laser pulses along the linear dispersion mode of a PBG bimodal waveguide. For all-optical switching [13,14], these are control laser pulses, while for the all-optical logic, these are holding and signal pulses. The probe pulses in both the switching and logic devices propagate in the linear dispersion mode. In addition to the linear dispersion mode, the waveguide has a cutoff mode with cutoff frequency ω_C slightly below the laser carrier frequencies ω_{L_1,L_2} The waveguide is embedded with a distributed collection of inhomogeneously broadened two-level quantum dots. We denote the transition frequency of the mth quantum dot as ω_{A_m}. This frequency obeys a Gaussian distribution with mean $\overline{\omega}_A$ (near resonant with ω_L), with standard deviation σ_A.

The quantum dots are simultaneously driven by external picosecond laser pulses and internal radiation fields emitted by the dots into the linear and cutoff modes. The dots are also coupled to the structured electromagnetic vacuum, characterized by a sharp local density of states (LDOS) jump at ω_C due to the mode cutoff. This LDOS jump is modeled by two radiative decay parameters for the high and low LDOS regions, respectively. We assume the QDs are independent of each other and ignore any direct dipole-dipole interactions between them. This allows the evolution of each QD to be described individually. The individual responses are then summed up to form the net polarization field. The radiation field, including both the input laser pulses and dot emitted fields (in the linear and cutoff mode), propagate according to Maxwell's equations inside the waveguide. The Bloch equation and Maxwell equation are coupled through dipolar interactions between the dots and the total radiation field. Together they govern the complete semiclassical nonlinear dynamics of the all-optical switching and logic devices.

A. Bloch equations for two-level QDs

Assuming independent quantum dots, we model the evolution of each dot (a two-level system) interacting with the laser pulses and cumulative radiated field of the dots in the structured EM vacuum. The aggregate dipole of all quantum dots placed along the waveguide, each with a distinct transition frequency sampled from a Gaussian distribution, is used to form the macroscopic polarization field in the waveguide. This oscillating polarization field acts as the source of dipolar radiation into the waveguide modes. This radiation source term is incorporated into the Maxwell equation in the next section.

Consider a two-level quantum dot with transition frequency ω_{A_m} detuned slightly from a step discontinuity in the electromagnetic density of states at frequency ω_C (provided by the waveguide cutoff mode), interacting simultaneously with electromagnetic fields in a linear dispersion mode with a strong component $E_{L_1}(t)$ and a weak component $E_{L_2}(t)$, as well as another weak field $E_C(t)$ in a waveguide cutoff mode. The central frequencies of these fields are $\omega_{L_1,L_2,C}$ and their slowly varying envelop functions are denoted as $\tilde{E}_{L_1,L_2,C}(t)$, respectively. In addition, the two-level system interacts with a smooth featureless nonradiative reservoir that is statistically independent from the photonic reservoir. This coupling to phonons causes dephasing of the atomic dipole. The contributions of the two reservoirs to the evolution of the reduced density operator of the two-level system are assumed to factorize and are treated separately.

We assume the following form of the EM waves in the linear and cutoff mode:

$$\begin{aligned} E_{L_1,L_2}(x,t) &= \tilde{E}_{L_1,L_2}(x,t)e^{-i(\omega_{L_1,L_2}t-k_{L_1,L_2}x)} + \text{c.c.},\\ E_C(x,t) &= \tilde{E}_C(x,t)(e^{-i(\omega_C t-k_C x)} + e^{-i(\omega_C t+k_C x)}) + \text{c.c.} \end{aligned} \tag{1}$$

In general, both $\tilde{E}_{L_1,L_2}(x,t)$ and $\tilde{E}_C(x,t)$ can be written as

$$\begin{aligned} \tilde{E}_{L_1,L_2}(x,t) &= |\tilde{E}_{L_1,L_2}(x,t)|e^{-i\tilde{\phi}_{L_1,L_2}},\\ \tilde{E}_C(x,t) &= |\tilde{E}_C(x,t)|e^{-i\tilde{\phi}_C}. \end{aligned} \tag{2}$$

The Hamiltonian of a driven single QD located at x (in the absence of phonon coupling) consists of three parts:

$$H = H_S + H_R + H_{SR}. \tag{3}$$

H_S is the Hamiltonian of the field-driven atom, H_R describes the electromagnetic reservoir, and H_{SR} is the atom-reservoir coupling. In the bare atomic basis (ground state $|1\rangle$ and excited state $|2\rangle$), this Hamiltonian [in rotating wave approximation (RWA) in the linear dispersion mode rotating frame $e^{-i(\omega_{L_1}t-k_{L_1}x)}$] takes the form

$$\begin{aligned} H_S &= \tfrac{1}{2}\hbar\Delta_{A_mL_1}\sigma_3^{L_1} - \hbar(\epsilon_{L_1}+\epsilon_{L_2}+\epsilon_C)\sigma_{21}^{L_1}\\ &\quad -\hbar(\epsilon_{L_1}^\dagger+\epsilon_{L_2}^\dagger+\epsilon_C^\dagger)\sigma_{12}^{L_1},\\ H_R &= \sum_\lambda \hbar\omega_\lambda a_\lambda^\dagger a_\lambda,\\ H_{SR} &= i\hbar\sum_\lambda g_\lambda\left(a_\lambda^\dagger\sigma_{12}^{L_1} - a_\lambda\sigma_{21}^{L_1}\right). \end{aligned} \tag{4}$$

Here the time-dependent Rabi frequencies of the linear and cutoff modes are defined as

$$\begin{aligned} \epsilon_{L_1} &= \tilde{\epsilon}_{L_1}e^{-i\tilde{\phi}_{L_1}} = \frac{|\tilde{E}_{L_1}|\mu}{\hbar}e^{-i\tilde{\phi}_{L_1}},\\ \epsilon_{L_2} &= \tilde{\epsilon}_{L_2}e^{-i\phi_{L_2}} = \frac{|\tilde{E}_{L_2}|\mu}{\hbar}e^{-i\phi_{L_2}},\\ \epsilon_C &= \tilde{\epsilon}_C(e^{-i\phi_{C,1}}+e^{-i\phi_{C,-1}}) = \frac{|\tilde{E}_C|\mu}{\hbar}(e^{-i\phi_{C,1}}+e^{-i\phi_{C,-1}}), \end{aligned} \tag{5}$$

where $\phi_{L_2} = \delta\omega_{L_2}t - \delta k_{L_2}x + \tilde{\phi}_{L_2}$, $\phi_{C,1} = \delta\omega_C t - \delta k_C x + \tilde{\phi}_C$, and $\phi_{C,-1} = \delta\omega_C t + (k_C+k_L)x + \tilde{\phi}_C$, with $\delta\omega_{L_2} = \omega_{L_2} - \omega_{L_1}$, $\delta k_{L_2} = k_{L_2} - k_{L_1}$, $\delta\omega_C = \omega_C - \omega_{L_1}$, and $\delta k_C = k_C - k_{L_1}$. We assume the dipole moment transition element μ is real, and that the dipole is parallel to the pulse polarization for simplicity. $a_\lambda^\dagger$ and a_λ are the creation and annihilation operators of mode λ of the electromagnetic reservoir with frequency ω_λ. We define the detunings $\Delta_{A_mL_1} = \omega_{A_m} - \omega_{L_1}$, $\Delta_\lambda = \omega_\lambda - \omega_{L_1}$, and define the bare atomic operators in the linear dispersion mode rotating frame $e^{-i(\omega_{L_1}t-k_{L_1}x)}$ as $\sigma_{ij}^{L_1} = |i\rangle\langle j|$ $(i,j=1,2)$ for the dipoles, $\sigma_3^{L_1} = \sigma_{22}^{L_1} - \sigma_{11}^{L_1}$ for the population inversion, as well as in-phase and in-quadrature parts of the dipole moment:

$$\sigma_1^{L_1} = \sigma_{12}^{L_1} + \sigma_{21}^{L_1}, \quad \sigma_2^{L_1} = i\left(\sigma_{12}^{L_1} - \sigma_{21}^{L_1}\right). \tag{6}$$

The expectation values of the atomic operators are defined as $u_{L_1} = \langle\sigma_1^{L_1}\rangle$, $v_{L_1} = \langle\sigma_2^{L_1}\rangle$, and $w_{L_1} = \langle\sigma_3^{L_1}\rangle$. As a result of our independent QD assumption, each single QD is described separately by a set of Bloch equations. We incorporate inhomogeneous broadening by assuming a Gaussian distribution in dot transition frequency. For every spatial point along the waveguide, we calculate the average dipole moment and population $\overline{u}_{L_1}$, $\overline{v}_{L_1}$, and $\overline{w}_{L_1}$ by dividing the inhomogeneous distribution into a set of many equally separated frequency intervals. Each interval is assumed to support a distinct dot detuning $\Delta_{A_mL_1}$ at the center of the intervals. All QDs within this region are described by a representative Bloch vector whose dynamics obeys the set of Bloch equations with the central detuning $\Delta_{A_mL_1}$. Finally, $\overline{u}_{L_1}$, $\overline{v}_{L_1}$, and $\overline{w}_{L_1}$ are calculated as weighted averages of these representative

Bloch vectors, with their weights equaling the probability of a QD transition frequency falling within each of the frequency intervals.

1. Bloch equation for all-optical switching

Figure 2 shows a schematic spectral model of our proposed all-optical switching device. For simulation of all-optical switching we set $E_{L_2} = 0$, and assume that the cutoff field is generally much weaker than the laser field E_{L_1} in the linear dispersion mode. To simplify notations we denote $E_{L_1} = E_L$, $\omega_{L_1} = \omega_L$, $k_{L_1} = k_L$, and similarly replace all relevant subscripts and superscripts of L_1 with L. In this configuration, two electromagnetic fields drive the QD evolution near the LDOS discontinuity. According to Ref. [15], if one of the field components (the cutoff mode) is much weaker than the other (the linear dispersion mode) $|\epsilon_C| \ll |\epsilon_L|$, then the QD fluorescence spectrum is confined in the three regions ω_L and $\omega_L \pm 2\Omega_L$ of the central, left, and right Mollow sidebands of the linear dispersion mode (Ω_L is the generalized Rabi frequency of the linear dispersion mode E_L). In this situation, the QD master equation and resulting Bloch equation are derived in the dressed state basis of the linear dispersion mode E_L. The cutoff mode field is a time dependent perturbation on the singly driven dressed states. This assumption leads to the following time-dependent dressed states $|\tilde{1}\rangle_L$ and $|\tilde{2}\rangle_L$ that diagonalizes H_S,

$$|\tilde{1}\rangle_L = c_L(t)|1\rangle + s_L(t)|2\rangle, \quad |\tilde{2}\rangle_L = -s_L(t)|1\rangle + c_L(t)|2\rangle, \tag{7}$$

where

$$\begin{aligned} c_L^2(t) &= \{1 + \Delta_{A_m L}/[2\Omega_{LC}(t)]\}/2, \\ s_L^2(t) &= \{1 - \Delta_{A_m L}/[2\Omega_{LC}(t)]\}/2, \\ \Omega_{LC}(t) &= \left[\left(\Delta_{A_m L}/2\right)^2 + |\epsilon_L + \epsilon_C|^2\right]^{1/2}. \end{aligned} \tag{8}$$

The dressed state atomic operators are defined similarly as their bare state counterparts:

$$\tilde{R}_{ij}^L = |\tilde{i}\rangle_L\langle\tilde{j}|_L \quad (i,j = 1, 2), \quad \tilde{R}_3^L = \tilde{R}_{22}^L - \tilde{R}_{11}^L.$$

By working in the dressed state basis Eq. (7), the Bloch equations of the mth single QD at position x near the LDOS discontinuity, doubly driven by fields of both the linear and the cutoff modes, can be derived in the rotating frame of $e^{-i(\omega_L t - k_L x)}$ [15]. When transferred back to the bare atomic basis, the Bloch equations have the form Ref. [15]

$$\begin{aligned} \dot{u}_L &= -\Delta_{A_m L} v_L - \frac{1}{T_u^L} u_L + V_L \\ &\quad - 2[\tilde{\epsilon}_L \sin\tilde{\phi}_L + \tilde{\epsilon}_C(\sin\phi_{C,1} + \sin\phi_{C,-1})]w_L, \\ \dot{v}_L &= \Delta_{A_m L} u_L - \frac{1}{T_v^L} v_L \\ &\quad + 2[\tilde{\epsilon}_L \cos\tilde{\phi}_L + \tilde{\epsilon}_C(\cos\phi_{C,1} + \cos\phi_{C,-1})]w_L, \\ \dot{w}_L &= -\frac{1}{T_w^L}(w_L + 1) + V_L u_L \\ &\quad - 2[\tilde{\epsilon}_L \cos\tilde{\phi}_L + \tilde{\epsilon}_C(\cos\phi_{C,1} + \cos\phi_{C,-1})]v_L \\ &\quad + 2[\tilde{\epsilon}_L \sin\tilde{\phi}_L + \tilde{\epsilon}_C(\sin\phi_{C,1} + \sin\phi_{C,-1})]u_L. \end{aligned} \tag{9}$$

Here $1/T_{u,v}^L = \frac{c_L^2(1+s_L^2)\gamma_+ + s_L^4\gamma_- + 4\gamma_p}{2} \mp \frac{c_L^2 s_L^2(\gamma_+ - \gamma_-)}{2}$ and $1/T_w^L = c_L^2(1 + s_L^2)\gamma_+ + s_L^4\gamma_-$ are field dependent relaxation rates. γ_- and γ_+ are the radiative decay rates at the high and low DOS regions, respectively, and γ_p is the nonradiative (phonon) dephasing rate. $V_L = (\gamma_+ - \gamma_-)c_L s_L^3$ is a "vacuum structure" term. T_u^L and T_v^L reduce to the transverse dephasing time, and T_w^L reduces to the longitudinal dephasing time in ordinary vacuum if we set $\gamma_+ = \gamma_-$.

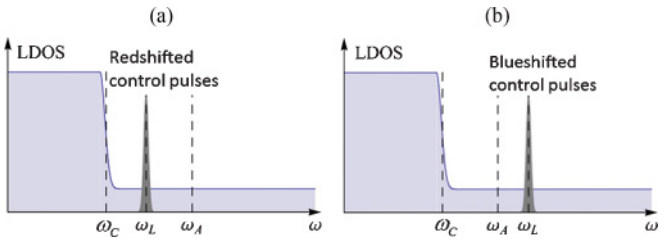

FIG. 2. (Color online) Schematic spectral model of an all-optical switching device. (a) Red-shifted control pulses excite the two-level QD medium to allow passage of subsequent signal pulses. (b) Blue-shifted control pulses deexcite the two-level QD medium to forbid passage of subsequent signal pulses.

2. Bloch equation for all-optical logic operations

Figure 3 shows a schematic spectral model of our proposed all-optical logic devices. For all-optical logic operations, two distinct wavelength channels of pulses propagate in the linear dispersion mode. We designate $E_{L_1} = E_h$ for the holding pulse channel, while $E_{L_2} = E_S$ is for the signal pulse channel. To simplify notations we also denote $\omega_{L_1} = \omega_h$, $\omega_{L_2} = \omega_S$, $k_{L_1} = k_h$, $k_{L_2} = k_S$, and similarly replace all relevant subscripts and superscripts of L_1 and L_2 with h and S, respectively. In this configuration, the QD is driven by three electromagnetic fields simultaneously, namely, the holding, signal, and cutoff mode fields. The fluorescence spectrum of QDs driven by three beams is more complex than that of only two driving fields, and the incoherent terms of the Bloch equation are not as simple as in Eq. (9). However (as confirmed in the following simulations) the QD radiation into the cutoff mode is much weaker than the other driving fields in the linear dispersion mode. In this situation, when deriving the incoherent part of the Bloch equation, we ignore the influence of the cutoff mode field on the QD dressed state. In other words, we assume the QD fluorescence spectrum is determined entirely by the holding and signal fields. If we further require that the signal field to be much weaker than the holding field $|\epsilon_S| \ll |\epsilon_h|$, then the fluorescence spectrum is confined in the three regions ω_h and $\omega_h \pm 2\Omega_h$ of the central, left, and right Mollow sidebands of the holding pulse (Ω_h is the generalized Rabi frequency of the holding pulse E_h). We treat the signal field as a time-dependent perturbation on the singly driven dressed states of the holding field. This assumption leads to the following time-dependent dressed states $|\tilde{1}\rangle_h$ and $|\tilde{2}\rangle_h$,

$$\begin{aligned} |\tilde{1}\rangle_h &= c_h(t)|1\rangle + s_h(t)|2\rangle, \\ |\tilde{2}\rangle_h &= -s_h(t)|1\rangle + c_h(t)|2\rangle, \end{aligned} \tag{10}$$

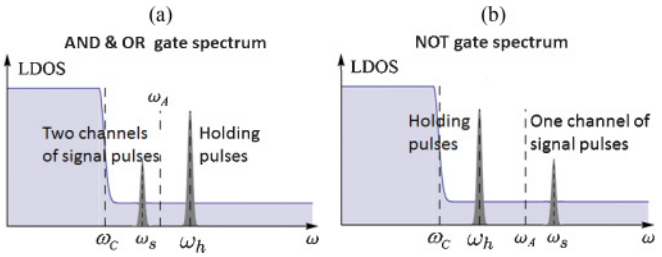

FIG. 3. (Color online) Spectral configuration of the logic (a) AND, OR, and (b) NOT devices.

where

$$c_h^2(t) = \{1 + \Delta_{A_m h}/[2\Omega_{hS}(t)]\}/2,$$
$$s_h^2(t) = \{1 - \Delta_{A_m h}/[2\Omega_{hS}(t)]\}/2, \quad (11)$$
$$\Omega_{hS}(t) = \{(\Delta_{A_m h}/2)^2 + |\epsilon_h + \epsilon_S|^2\}^{1/2}.$$

The dressed state atomic operators are defined similarly as their bare state counterparts:

$$\tilde{R}^h_{ij} = |\tilde{i}\rangle_h\langle\tilde{j}|_h \quad (i,j = 1,2), \quad \tilde{R}^h_3 = \tilde{R}^h_{22} - \tilde{R}^h_{11}.$$

By working in the dressed state basis Eq. (10), the Bloch equations in the rotating frame of $e^{-i(\omega_h t - k_h x)}$ of the mth QD at position x, driven by fields of the linear and the cutoff modes, can be derived [15]. To simplify the derivation of the incoherent part of the Bloch equation, we ignored the effect of the cutoff mode on the dressed state spectrum. However, the coherent driving terms of the cutoff mode EM field are easily evaluated (as cross products of the Bloch vector with the cutoff mode torque vector). Since these terms may influence the coherent Bloch dynamics, we explicitly include them in the Bloch equation. When transformed back to the bare atomic basis, the Bloch equations become

$$\begin{aligned}
\dot{u}_h &= -\Delta_{A_m h} v_h - \frac{1}{T_u} u_h + V \\
&\quad - 2[\tilde{\epsilon}_h \sin\tilde{\phi}_h + \tilde{\epsilon}_S \sin\phi_S + \tilde{\epsilon}_C(\sin\phi_{C,1} + \sin\phi_{C,-1})]w_h, \\
\dot{v}_h &= \Delta_{A_m h} u_h - \frac{1}{T_v} v_h \\
&\quad + 2[\tilde{\epsilon}_h \cos\tilde{\phi}_h + \tilde{\epsilon}_S \cos\phi_S + \tilde{\epsilon}_C(\cos\phi_{C,1} + \cos\phi_{C,-1})]w_h, \\
\dot{w}_h &= -\frac{1}{T_w}(w_h + 1) + V u_h \\
&\quad - 2[\tilde{\epsilon}_h \cos\tilde{\phi}_h + \tilde{\epsilon}_S \cos\phi_S + \tilde{\epsilon}_C(\cos\phi_{C,1} + \cos\phi_{C,-1})]v_h \\
&\quad + 2[\tilde{\epsilon}_h \sin\tilde{\phi}_h + \tilde{\epsilon}_S \sin\phi_S + \tilde{\epsilon}_C(\sin\phi_{C,1} + \sin\phi_{C,-1})]u_h.
\end{aligned} \quad (12)$$

Here $1/T^h_{u,v} = \frac{c_h^2(1+s_h^2)\gamma_+ + s_h^4\gamma_- + 4\gamma_p}{2} \mp \frac{c_h^2 s_h^2(\gamma_+ - \gamma_-)}{2}$, $1/T^h_w = c_h^2(1+s_h^2)\gamma_+ + s_h^4\gamma_-$, and $V_h = (\gamma_+ - \gamma_-)c_h s_h^3$.

B. Envelope equations of the waveguide modes

The propagation of electromagnetic fields in the waveguide is described by the Maxwell's equation inside the photonic crystal with the polarization field $P(x,t)$ of embedded two-level QDs acting as the source term. To fully describe the pulse propagation inside the waveguide, a detailed modeling of the PBG waveguide dielectric structure in 3D is required. However, in this article we abstract the key properties of the PBG waveguide to simplify the problem. In the following we reduce the waveguide to a one-dimensional system and derive the electromagnetic envelope equation in the linear and cutoff modes, respectively. The envelope equations contain fitting parameters that allow an approximate description of the dispersion curves of a realistic 3D-PBG waveguide structure.

In reducing the 3D problem into 1D, we approximate the actual transverse field distribution with a simplified one. We assume the field is uniform along the cross-sectional directions of the waveguide and that it vanishes outside the waveguide. This corresponds to assuming a uniform overlap of the field with all QDs embedded in a given cross-sectional plane of the waveguide. For a typical bimodal waveguide in a 2D-3D PBG heterostructure, using light with 1500 nm vacuum wavelength, the lattice constant of the PC is $a \approx 600$ nm, and the cross-sectional area of the waveguide is approximately $(a/3) \times (3a) = a^2$ [16].

1. Envelope equation of the linear dispersion EM modes

We model the input pulses in the linear dispersion mode of the waveguide as propagating through an effective one-dimensional system, obeying the Maxwell equation with a source term coming from the polarization field P of the embedded two-level QDs,

$$\frac{\partial^2 E_{L_1,L_2}}{\partial x^2} - \frac{\varepsilon_{\text{eff}}(x)}{c^2}\frac{\partial^2 E_{L_1,L_2}}{\partial t^2} = \frac{4\pi}{c^2}\frac{\partial^2 P}{\partial t^2}. \quad (13)$$

Here $\varepsilon_{\text{eff}}(x)$ is the effective dielectric structure giving rise to the linear dispersion curve being modeled around ω_{L_1,L_2}.

As discussed previously, in the static frame, we assume the electric field of the linear dispersion mode has the form

$$E_{L_1,L_2} = \tilde{E}_{L_1,L_2}(x,t)e^{-i(\omega_{L_1,L_2}t - k_{L_1,L_2}x)} + \text{c.c.} \quad (14)$$

Here ω_{L_1,L_2} and k_{L_1,L_2} are the carrier frequency and wave vector of the propagating pulses. Although the dispersion curve is approximately linear around ω_{L_1,L_2}, the group velocity v_g characterizing the speed of the envelope function $\tilde{E}_{L_1,L_2}(x,t)$ (in the absence of embedded QDs) need not coincide with the phase velocity $v_p = \omega_{L_1}/k_{L_1} = \omega_{L_2}/k_{L_2}$. ω_{L_1,L_2}, k_{L_1,L_2}, and v_g remain independent parameters determined by the detailed photonic-crystal waveguide architecture.

In the static frame, the polarization P of the QD medium can be expressed as

$$\begin{aligned}
P(x,t) &= \mu n(\langle\sigma_{12}\rangle_{\text{avg}} + \text{c.c.}) \\
&= \mu n\left(\langle\tilde{\sigma}_{12}^{L_1,L_2}\rangle e^{-i(\omega_{L_1,L_2}t - k_{L_1,L_2}x)} + \text{c.c.}\right),
\end{aligned} \quad (15)$$

where $\langle\sigma_{12}\rangle_{\text{avg}}$ is the average expected value of the QD dipole in the static frame. $\langle\tilde{\sigma}_{12}^{L_1,L_2}\rangle$ are the envelope functions of $\langle\sigma_{12}\rangle_{\text{avg}}$ when viewed from the $e^{-i(\omega_{L_1,L_2}t - k_{L_1,L_2}x)}$ rotating frame. μ is the single QD dipole transition matrix element and n is the number density of QDs. Since the QDs interact nonlinearly with the linear dispersion and cutoff modes simultaneously, $\langle\sigma_{12}\rangle_{\text{avg}}$ has fast oscillating components at both ω_{L_1,L_2} and ω_C frequencies, as well as other frequency components (e.g., Rabi frequency components and higher order harmonics, etc.).

To estimate the QD number density, following Ref. [17], we assume the average QD has a pyramidal shape with base

15 nm by 15 nm, and height 7 nm. Assuming the QDs are spaced 5 nm away from each other in all three dimensions, then their number density is roughly $n = 2 \times 10^5\ \mu\text{m}^{-3}$, which will be used for all the simulations presented below. The dipole moment matrix element of the dots are chosen to be $\mu = 3.33 \times 10^{-22}$ C μm (100 D), which has been demonstrated in Refs. [23–25].

The envelop function $\langle\tilde{\sigma}_{12}^{L_1}\rangle$ can be expressed in terms of the average Bloch vector $\overline{\boldsymbol{\rho}} = (\overline{u}_{L_1}, \overline{v}_{L_1}, \overline{w}_{L_1})$ [obeying Eq. (9) or (12)]:

$$\left\langle\tilde{\sigma}_{12}^{L_1}\right\rangle = (\overline{u}_{L_1} - i\overline{v}_{L_1})/2. \tag{16}$$

The envelop function $\langle\tilde{\sigma}_{12}^{L_2}\rangle$, on the other hand, is given by

$$\left\langle\tilde{\sigma}_{12}^{L_2}\right\rangle = \frac{\overline{u}_{L_1} - i\overline{v}_{L_1}}{2e^{-i(\delta\omega_{L_2}t - \delta k_{L_2}x)}}. \tag{17}$$

We assume that the electric field in the linear dispersion mode is of the form Eq. (14) and the polarization of the QD medium is of the form Eq. (15). The envelope function $\tilde{E}_{L_1,L_2}$ is slowly varying both temporarily and spatially, and propagates forward with speed v_g. Therefore we model the movement of $\tilde{E}_{L_1,L_2}$ with an effective homogeneous medium whose dielectric constant produces the group velocity v_g (slope of the dispersion curve). On the other hand, the phase velocity is independently modeled through the phase factor $e^{-i(\omega_{L_1,L_2}t - k_{L_1,L_2}x)}$ by the actual frequency ω_{L_1,L_2} and wave vector k_{L_1,L_2} of the pulses. v_g, ω_{L_1,L_2}, and k_{L_1,L_2} forms the set of independent parameters that we use to model the linear dispersion mode in which our pulses propagate. Then by making the slowly varying envelop approximation, we obtain the following wave equations for the envelope function (see Appendix A for details):

$$\frac{\partial\tilde{E}_{L_1,L_2}}{\partial x} + \frac{1}{v_g}\frac{\partial\tilde{E}_{L_1,L_2}}{\partial t} + \frac{\Gamma_L}{v_g}\tilde{E}_{L_1,L_2} = \frac{2i\pi\mu n\omega_{L_1,L_2}v_g}{c^2}\left\langle\tilde{\sigma}_{12}^{L_1,L_2}\right\rangle. \tag{18}$$

Here a broad band linear loss rate Γ_L is included as well. This Γ_L can describe either additional absorption losses or decay of the optical mode from a finite segment of the PBG waveguide.

2. *Envelope equation of the cutoff mode*

Near ω_C, the cutoff mode dispersion curve can be approximated by a parabola whose curvature describes the photon effective mass. Following the approach of Refs. [21] and [22], we model the cutoff mode as the lower band edge of a one-dimensional photonic crystal with periodic dielectric constant $\varepsilon(x) = \overline{\varepsilon} + \Delta\varepsilon\cos(2k_Cx)$, where $\overline{\varepsilon}$ is the average dielectric constant and $\Delta\varepsilon$ is the spatial dielectric modulation amplitude at wave vector k_C. As with the linear dispersion mode, the Maxwell equation for EM wave $E_C(x,t)$ in this mode also has a source term coming from the polarization P of the embedded two-level QDs:

$$\frac{\partial^2E_C}{\partial x^2} - \frac{\varepsilon(x)}{c^2}\frac{\partial^2E_C}{\partial t^2} = \frac{4\pi}{c^2}\frac{\partial^2P}{\partial t^2}. \tag{19}$$

At the immediate vicinity of ω_C, the electric field $E_C(x,t)$ of the cutoff mode can be written in terms of its envelope function $\tilde{E}_C(x,t)$ as

$$E_C(x,t) = \tilde{E}_C(x,t)(e^{-i(\omega_Ct - k_Cx)} + e^{-i(\omega_Ct + k_Cx)}) + \text{c.c.} \tag{20}$$

By expressing the dispersion curve of this one-dimensional system in a quadratic form near the lower band edge (with frequency and wave vectors scaled with ω_C^{-1} and k_C^{-1}, respectively) [21,22], we obtain the simplified dispersion for a negative effective mass particle:

$$(\omega - \omega_C)/\omega_C = -\frac{1}{2\beta}\left(\frac{q - k_C}{k_C}\right)^2 + \text{higher order terms}. \tag{21}$$

Here $\beta = \Delta\varepsilon/4\overline{\varepsilon}$. Following the approach of Refs. [21] and [22], we obtain the following Schrödinger-like equation for $\tilde{E}_C(x,t)$ in the effective mass approximation:

$$i\frac{\partial\tilde{E}_C}{\partial t} - \frac{1}{2\beta}\frac{\partial^2\tilde{E}_C}{\partial x^2} + (\beta + i\Gamma_C)\tilde{E}_C + \frac{2\pi n\mu}{\overline{\varepsilon}}\left\langle\tilde{\sigma}_{12}^{C}\right\rangle = 0. \tag{22}$$

Here the envelope equation $\langle\tilde{\sigma}_{12}^{C}\rangle$ of the QD polarization,when viewed from the cutoff mode frame, can be expressed as (see Appendix B)

$$\left\langle\tilde{\sigma}_{12}^{C}\right\rangle = \frac{\overline{u}_{L_1} - i\overline{v}_{L_1}}{2(e^{-i(\delta\omega_Ct - \delta k_Cx)} + e^{-i[\delta\omega_C + (k_C + k_{L_1})x]})}. \tag{23}$$

As in Eq. (18), we introduce another decay parameter Γ_C describing either intrinsic absorption loss or leakage of the optical energy from a finite length segment of the PBG waveguide.

III. SIMULATION OF PULSE PROPAGATION

For numerical simplicity we rewrite the linear dispersion field envelope equation (18) in terms of the linear dispersion mode Rabi frequency by multiplying the equation by $\mu/\hbar$, and converting to international SI unit:

$$\frac{\partial\epsilon_{L_1,L_2}}{\partial x} + \frac{1}{v_g}\frac{\partial\epsilon_{L_1,L_2}}{\partial t} + \frac{\Gamma_L}{v_g}\epsilon_{L_1,L_2} = i\frac{n\omega_{L_1,L_2}\mu^2}{2\varepsilon v_g\varepsilon_0\hbar}\left\langle\tilde{\sigma}_{12}^{L_1,L_2}\right\rangle. \tag{24}$$

The cutoff mode envelope Eq. (22) is treated similarly. However, the cutoff mode Rabi frequency defined in Eq. (5) is expressed in the linear dispersion mode rotating frame, while Eq. (22) is derived in the frame of the cutoff mode. Therefore, we define $\epsilon_C' = \mu\tilde{E}_C/\hbar = \mu|\tilde{E}_C|e^{-i\phi_C}/\hbar$ as Rabi frequency in the cutoff mode frame, so that (also in SI units)

$$i\frac{\partial\epsilon_C'}{\partial t} - B\frac{\partial^2\epsilon_C'}{\partial x^2} + \left[\frac{1}{2B}\left(\frac{\omega_C}{k_C}\right)^2 + i\Gamma_C\right]\epsilon_C' + \frac{n\omega_C\mu^2}{2\varepsilon_0\overline{\varepsilon}\hbar}\left\langle\tilde{\sigma}_{12}^{C}\right\rangle = 0. \tag{25}$$

Here $B = \frac{\omega_C}{2\beta k_C^2}$ is the coefficient of the quadratic term in the dispersion relation (21) when expressed in unscaled form

$$(\omega - \omega_C) = -B(q - k_C)^2 + \text{higher order terms}. \tag{26}$$

ϵ_{L_1,L_2} and ϵ'_C that appear in Eqs. (24) and (25) are in general complex, and have the same dimension as the field Rabi frequency variables $\tilde{\epsilon}_{L_1,L_2,C}$ appearing in the Bloch equation (9) or (12). These variables are related as

$$\begin{aligned} \tilde{\epsilon}_{L_1,L_2} &= |\epsilon_{L_1,L_2}|, \quad \tilde{\epsilon}_C = |\epsilon'_C|, \quad \tilde{\phi}_{L_1} = -\mathrm{Arg}(\epsilon_{L_1}), \\ \phi_{L_2} &= \delta\omega_{L_2} t - \delta k_{L_2} x - \mathrm{Arg}(\epsilon_{L_2}), \\ \phi_{C,1} &= \delta\omega_C t - \delta k_C x - \mathrm{Arg}(\epsilon'_C), \\ \phi_{C,-1} &= \delta\omega_C t + (k_C + k_L)x - \mathrm{Arg}(\epsilon'_C), \end{aligned} \tag{27}$$

where $\mathrm{Arg}(x)$ is the angle of a complex quantity x. Equation (9) (for optical switching) or (12) (for optical logic), (16), (17), (23), (24), (25), and (27) form the closed set of equations for numerical simulation of pulse propagation inside the bimodal PBG waveguide.

We assume the input pulse enters the linear dispersion mode of the waveguide at time $t = 0$ through $x = 0$, and propagates along the positive x direction. The boundary conditions for the linear dispersion mode envelope equation (24) at $x = 0$ are therefore specified as the external input pulse envelope functions $\tilde{E}_{L_1,L_2}(x = 0,t) = \tilde{E}_{L_1,L_2}(t)$. These are assumed to be Gaussian pulses in this article. Neumann boundary conditions [26] are specified for the cutoff mode envelope equation (25) at both the $x = 0$ and $x = x_{\max}$ boundaries. The quantum dots inside the waveguide have an initial Bloch vector profile $\boldsymbol{\rho}(x,t = 0) = \boldsymbol{\rho}_0(x)$, and no initial electromagnetic field exists inside either the linear or the cutoff mode of the waveguide [$\tilde{E}_{L_1,L_2,C}(x,t = 0) = 0$].

Finite difference schemes are employed to solve the coupled Maxwell-Bloch equations, including implicit Euler [26] scheme for the linear dispersion mode envelope (24), Crank Nicolson scheme [26] for the cutoff mode envelope (25), and explicit Euler [26] for the Bloch equations (9) and (12). The dipole moment averages $\overline{u}_L$ and $\overline{v}_L$ that appear in Eqs. (16), (17), and (23) are calculated by dividing the frequency region $[\overline{\omega}_A - N_\sigma\sigma_A, \overline{\omega}_A + N_\sigma\sigma_A]$ of the QD transition frequency distribution (here σ_A is the standard deviation of the Gaussian QD transition frequency distribution, and N_σ represents the number of standard deviations included in the simulation) into a number N_A (typically $N_A = 20$ in our simulation) of equally spaced narrow frequency regions $[\omega_{A_l},\omega_{A_{l+1}}]$ ($l = 1,2,\ldots,N_A$, and $\omega_{A_1} = \overline{\omega}_A - N_\sigma\sigma_A$, $\omega_{A_{N_A+1}} = \overline{\omega}_A + N_\sigma\sigma_A$). Each frequency interval corresponds to a distinct, representative dot transition frequency $\omega_{A_m} = (\omega_{A_l} + \omega_{A_{l+1}})/2$ at the center of this region. All QDs within this region are then described by the representative Bloch vector whose dynamics obey the set of Bloch equations (9) or (12), at transition frequency detuning $\Delta_{A_m L_1} = \omega_{A_m} - \omega_{L_1}$. $\overline{u}_{L_1}, \overline{v}_{L_1}$, and $\overline{w}_{L_1}$ are then taken as the weighted averages of these N_A representative Bloch vectors, with the weights being the probability of the QD transition frequencies falling within the corresponding frequency region $[\omega_{A_l},\omega_{A_{l+1}}]$. For notational simplicity we denote $\overline{u}_{L_1}$, $\overline{v}_{L_1}$, and $\overline{w}_{L_1}$ as $\overline{u}$, $\overline{v}$, and $\overline{w}$ from now on.

A. Self-induced transparency in an unstructured vacuum

As a consistency check of our numerical scheme, we reproduce the well known results of self-induced transparency (SIT) [27] in this section.

Self-induced transparency occurs when an intense coherent electromagnetic pulse propagates inside a resonant absorbing medium with little or no attenuation, in the form of a stable soliton. It happens when the pulse duration is much shorter than the inverse inhomogeneous broadening linewidth of the medium and the accumulated pulse strength satisfies certain conditions [27]. We define the area of the input laser pulse $E_L(x,t)$ at x as

$$\theta_L(x) = 2\int_{-\infty}^{\infty} \epsilon_L(x,t)dt. \tag{28}$$

Then if $\theta_L < \pi$, the pulse attenuates with increasing travel distance x. If $\pi < \theta_L < 3\pi$, the pulse will evolve into a stable hyperbolic secant pulse of area 2π and pass through the medium without attenuation. Pulses with area above 3π will be unstable and breaks into multiple pulses as they propagate.

To simulate SIT, we remove the cutoff mode from the Maxwell-Bloch equations (since no such mode exists in ordinary vacuum), set $E_{L_2} = 0$, $E_{L_1} = E_L$, $\gamma_+ = \gamma_- \ll 1/\tau$ (τ being the input pulse duration), $\Delta_{AL} = 0$, and $\sigma_A \gg 1/\tau$. This reduces our system to a one-dimensional, resonant pulse propagation problem inside an inhomogeneously broadened two-level medium in ordinary vacuum. The Bloch vector of each single QD satisfies Bloch equation (9). Figure 4 shows the simulation result of a 0.8π and a 1.4π pulse entering the medium at $x = 0$ and propagating along the positive x direction. The 0.8π pulse attenuates to eventually vanish at about $x = 10$ μm as it propagates forward [Fig. 4(a)]. The plot of average population inversion in the medium as function of x and t [Fig. 4(c)] also confirms the gradual disappearance of the pulse with increasing x. On the other hand, the 1.4π pulse is reshaped along the way to a stable shape at about $x = 5$ μm

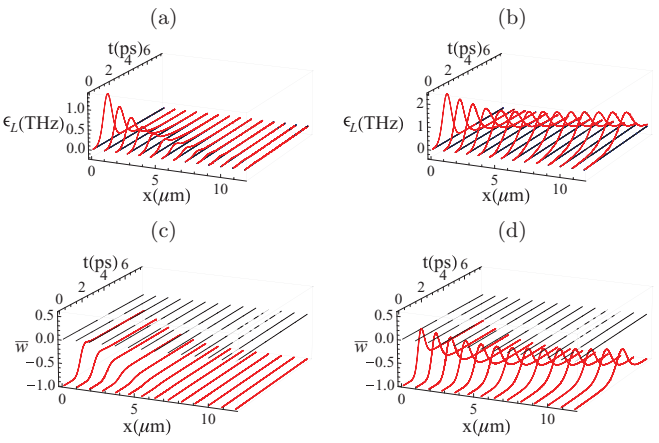

FIG. 4. (Color online) Resonant pulse propagation in an inhomogeneously broadened two-level medium in ordinary vacuum. This figure recaptures the SIT phenomena where a 0.8π pulse is gradually absorbed during propagation, while a 1.4π pulse evolves into a stable 2π pulse. $v_g = 0.2c$, $\tau = 1$ ps, $\gamma_{\text{high}} = \gamma_{\text{low}} = \gamma_p = 0$, $n = 2 \times 10^5$ μm^{-3}, $\mu = 3.33 \times 10^{-22}$ μm C (100 D), $\overline{\Delta}_{AL} = 0$, $\sigma_A = 5$ THz (corresponding to 12 THz of distribution width at full-width half-maximum, or about 1% for QD transitions centered at 1.5 μm), $N_\sigma = 3$, $N_A = 20$, $\boldsymbol{\rho}_0 = (0,0,-1)$. (a) and (b) Evolution of 0.8π and 1.4π pulse amplitudes (Rabi frequencies), respectively. (c) and (d) Evolution of average population inversion of the two-level medium during passage of 0.8π and 1.4π pulses, respectively.

and keeps propagating forward without attenuation [Fig. 4(b)]. There are a several parameters for the QD medium and the host photonic-crystal waveguides, including n, μ, v_g, and $\gamma_\pm$, that determine this spatial length scale. This will be further discussed in Sec. III E. The corresponding average population plot [Fig. 4(d)] shows the area of the stable pulse established indeed has an area of 2π as $\overline{w}$ returns to the initial ground state after the pulse passage. This confirms that our numerical scheme recaptures SIT for an appropriate choice of parameters.

B. Pulse propagation inside an ultrafast all-optical switch

Now we apply our numerical scheme to simulate pulse propagation inside an all-optical switching device based on embedded QDs inside a PBG waveguide [13,14]. The pulse propagates along the linear dispersion mode of a bimodal PBG waveguide with LDOS discontinuity caused by the cutoff mode.

We consider electromagnetic wave propagation along the direction of the waveguide x only, without detailed treatment of the cross sectional distributions in the y and z directions. As stated earlier, we assume uniform field distribution along the cross-sectional directions of the waveguide. As such, in the envelope equations (24) and (25), we abstract mode characteristics most influential on wave propagation along the waveguide. We model dispersion relations directly and ignore details of the spatial mode structure, determined by the microscopic dielectric architecture. Nonetheless, to make our simulation more realistic, we estimate major parameters for the envelope equations (24) and (25) and Bloch equations (9) or (12) from a microscopically designed 2D-3D PBG heterostructure waveguide [16] that exhibits bimodal waveguide dispersion curves matching our model. This structure has also been studied earlier [13,14] to conceptually illustrate operation of a picosecond all-optical switching device.

The PBG waveguide structure presented in Ref. [16] was extensively studied using finite difference time domain (FDTD) simulations. This 3D-2D photonic-crystal heterostructure is composed of inverse square spiral structures as the 3D cladding layers and a square lattice of cylindrical rods comprising comprising the 2D microchip layer. Figure 3 of Ref. [16] shows the existence of two waveguide modes, one with linear dispersion and one cutoff mode, for a W3 waveguide within the PBG of this heterostructure.

The carrier frequency ω_L of the control pulse propagating in the linear dispersion mode is chosen to correspond to the vacuum wavelength of $\lambda = 1.5\ \mu$m so that $\omega_L = 2\pi c/\lambda = 1256.64$ THz. Then for ω_L to appear near the cutoff frequency ω_C at the middle of the on-chip PBG shown in Fig. 3(b) of Ref. [16], a lattice constant of $a \approx 0.555\ \mu$m is required. This allows us to determine $k_L \approx 0.33 \times 2\pi/a = 3.74\ \mu\text{m}^{-1}$ and $k_C \approx \pi/a = 5.66\ \mu\text{m}^{-1}$ according to the dispersion curves in Fig. 3(b) of Ref. [16].

The group velocity of the linear dispersion mode at the cutoff frequency is about $v_g = 0.24c$ with c being the vacuum speed of light. According to Eq. (A1) we model light propagation in this linear dispersion mode as that in a homogeneous medium with an effective dielectric constant determined from the group velocity $\epsilon = (c/v_g)^2 \approx 17.36$. We estimate the average dielectric constant $\overline{\epsilon}$ in Eq. (25) to be half of ϵ.

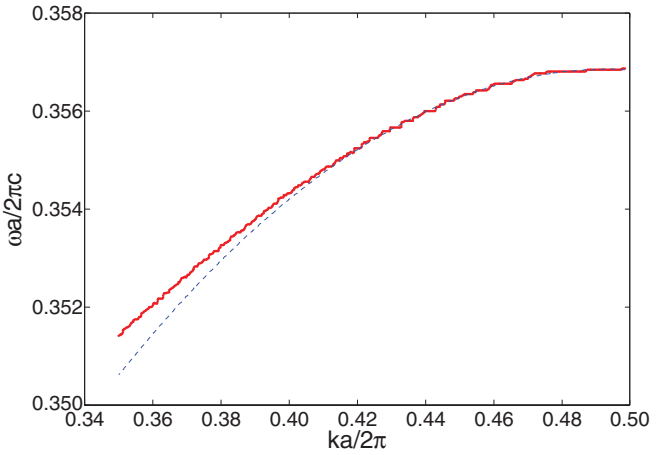

FIG. 5. (Color online) Quadratic fitting (dashed line) of the cutoff mode dispersion curve (solid line) near the cutoff frequency for the W3 waveguide specified in Fig. 3(b) of Ref. [16]. The dimensionless coefficient of the quadratic term from the fitting is $B_0 = 0.7546$. For a laser beam operating around 1.5 μm with $a \approx 0.555\ \mu$m, this corresponds to $B = B_0 ac/(2\pi) \approx 20\ \mu\text{m}^2\ \text{ps}^{-1}$.

One of the key parameters for the cutoff mode in Eq. (25) is the quadratic coefficient B of the dispersion curve. As shown in Fig. 5, this is estimated to be $B = 20\ \mu\text{m}^2\ \text{ps}^{-1}$ through a quadratic fitting of the cutoff dispersion curve shown in Fig. 3(b) of Ref. [16]. Due to finite length in real waveguide structures, the divergence of the cutoff mode LDOS peak is truncated, resulting in a finite FWHM of the peak. This effect is modeled as the linear loss rate Γ_C in Eq. (25). For a 15 unit cell long waveguide, $\Gamma_C = 1.88$ THz [13,14].

As a simulation of all-optical switching, Fig. 6 shows the spatial evolution of various picosecond Gaussian input pulses as they propagate along the waveguide with different initial QD average populations $\overline{w}(0)$. The probe pulse is sent in (beginning of probe simulation) immediately after the end of the control pulse simulation. Then according to Figs. 6(a) and 6(c), the temporal separation between the control and probe pulse peaks is 4.5 ps. The initial spatial population profile of the probe pulse is set to be the residual population profile of the control pulse. The evolution profiles of the QD population $\overline{w}$ under each of the situations in Fig. 6, as well as field emitted from the driven dots into the cutoff mode, are shown in Figs. 7 and 8, respectively.

A properly configured red-shifted control pulse can invert the QD medium [Figs. 6(a), 7(a), and 8(a)], thus allowing a subsequent resonant probe pulse to pass through the waveguide without attenuation [Figs. 6(c), 7(c), and 8(c)]. Figure 6(a) shows the evolution of the red-shifted control pulse propagating through the waveguide with the embedded QDs initially below inversion $\overline{w}(0) = -0.5$. The (red) thick and (blue) thin lines represent the real and imaginary parts of the pulse envelope function, respectively. The parameters used during simulation are detailed in the figure caption. As the control pulse evolves along the waveguide, an imaginary part of the envelope function emerges, reflecting a pulse phase shift. However, the overall pulse retains its shape over a distance of

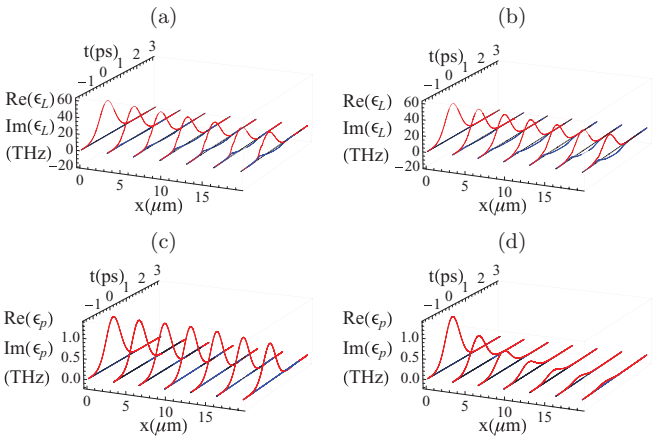

FIG. 6. (Color online) Simulated evolution of control or signal laser pulses along the waveguide inside an all-optical switching device. This figure shows that a red-shifted control pulse can allow a subsequent probe pulse to pass through without attenuation, while a blue-shifted control pulse can lead to absorbtion of a subsequent probe pulse. Thick (red) lines represent the real part of the pulse envelope functions, and thin (blue) lines represent the imaginary part of the envelope functions. $v_g = 0.24c$, $\tau = 1$ ps, $\Gamma_C = 1.88$ THz, $\Gamma_L = 2$ THz, $B = 20\,\mu\text{m}^2\,\text{ps}^{-1}$, $\gamma_{\text{high}} = 2.5$ THz, $\gamma_{\text{low}} = 5$ GHz, $\gamma_p = 0.5$ THz, $n = 2 \times 10^5\,\mu\text{m}^{-3}$, $\sigma_A = 5$ THz (about 1% for QD transitions centered at 1.5 μm), $N_\sigma = 4$, $N_A = 20$. (a) Dynamic inversion by red-shifted control pulse. $\epsilon_L^{\max} = 42$ THz, $\delta\omega_C = -5$ THz, $\overline{\Delta}_{AL} = 8$ THz, $\boldsymbol{\rho}_0 = (0,0,-0.5)$. (b) Dynamic deexcitation by blue-shifted control pulse. $\epsilon_L^{\max} = 42$ THz, $\delta\omega_C = -21$ THz, $\overline{\Delta}_{AL} = -8$ THz, $\boldsymbol{\rho}_0 = (0,0,0.2)$. (c) Probe pulse propagation after QD inversion. $\epsilon_p^{\max} = 1.18$ THz, $\delta\omega_C = -13$ THz, $\overline{\Delta}_{AL} = 0$. The initial average population is set to equal the final population in (a). (d) Probe pulse propagation after QD deexcitation. $\epsilon_p^{\max} = 1.18$ THz, $\delta\omega_C = -13$ THz, $\overline{\Delta}_{AL} = 0$. The initial average population is set to equal the final population in (b).

10–15 μm along the waveguide. Upon passage of this control pulse, the embedded QDs are mostly inverted into an active medium due to the structured vacuum [13,14]. This is seen from the average QD population $\overline{w}$ in Fig. 7(a). Although the final inversion level is nonuniform along the waveguide (due to control pulse shape changes during the propagation), the majority of the QDs remain excited with $\overline{w} > 0$. During the pulse passage along the linear dispersion mode, the QDs driven by the control pulse also radiate into the cutoff mode whose envelop function is shown in Fig. 8(a). The magnitude of the radiated field in the cutoff mode is much weaker than the input pulse in the linear dispersion mode. This is consistent with our assumption in obtaining the Bloch equation (9).

A resonant probe pulse sent after QDs inversion by the red-shifted control pulse can get amplified along the waveguide, as shown in Fig. 6(c). The energy is transferred from the QDs to the probe pulse, leaving the QDs at a lower excitation state after probe pulse passage, as seen in Fig. 7(c). The probe pulse is not significantly distorted over the 10–15 μm distance along the waveguide. The field emitted into the cutoff mode during passage of the probe pulse is also significantly weaker than the probe pulse itself, consistent with our assumption in Bloch equation (9).

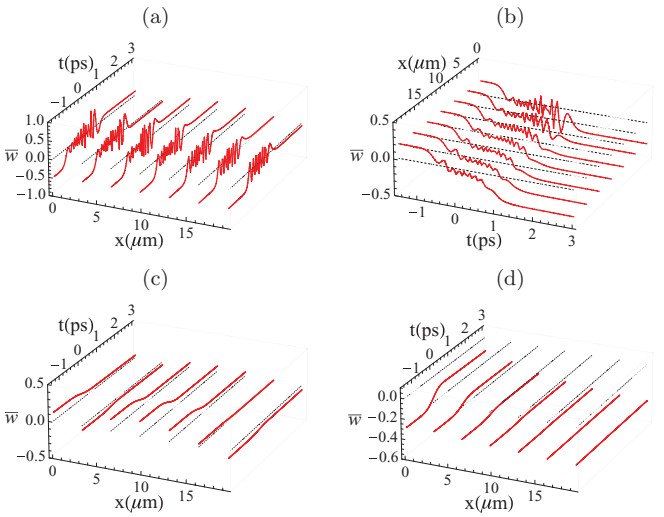

FIG. 7. (Color online) Simulated evolution of average QD population $\overline{w}(x,t)$ along the waveguide inside an all-optical switching device. Each graph shows QD population under the corresponding cases shown in Fig. 6, with the same parameters. This figure shows that (a) a red-shifted control pulse can invert the QD population, and (c) the inverted QDs are deexcited by the subsequent probe pulse. On the other hand, (b) a blue-shifted control pulse can deexcite the QD population, and (d) the resulted passive medium absorbs energy from the subsequent probe pulse.

On the other hand, a properly configured blue-shifted control pulse deexcites the QD medium [Figs. 6(b), 7(b), and 8(b)], leading to absorption of a subsequent resonant probe pulse [Figs. 6(d), 7(d), and 8(d)]. Figure 6(b) shows the evolution of the blue-shifted control pulse propagating through the waveguide with the embedded QDs initially above inversion $\overline{w}(0) = 0.2$. Similar to the red-shifted pulse, the envelope function of the blue-shifted control pulse also picks up an imaginary part as the pulse propagates through the waveguide. Overall, the pulse also keeps its shape over a

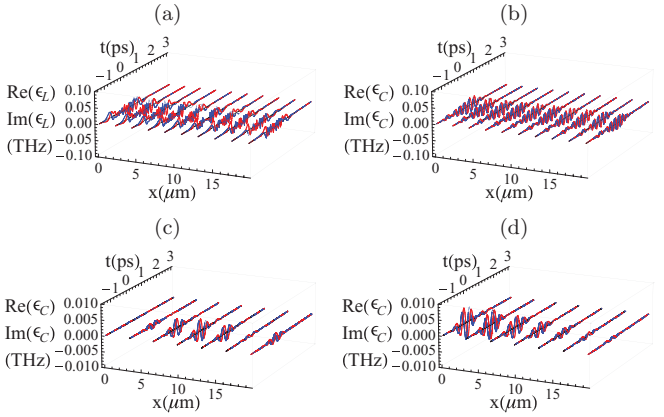

FIG. 8. (Color online) Simulated QD radiation into the cutoff mode along the waveguide during each of the corresponding all-optical switching actions shown in Fig. 6, with the same parameters. The radiated field strength is much weaker than that of the input control and signal pulses in the linear mode. Thick (red) lines represent the real part of the pulse envelope functions, and thin (blue) lines represent the imaginary part of the envelope functions.

distance of 10–15 μm along the waveguide. Upon passage of this control pulse, the embedded QDs are deexcited into a passive medium [13,14], as can be seen from the $\overline{w}$ evolution plot in Fig. 7(b) for QDs at different locations along the waveguide. The QD radiation field into the cutoff mode during the pulse passage is shown in Fig. 8(b). Its magnitude is also much weaker than that of the input pulse in the linear dispersion mode, consistent with assumption in the Bloch equation (9).

Although a resonant probe pulse sent after the red-shifted pulse can pass through the waveguide without attenuation, the same probe pulse sent after the blue-shifted control pulse is absorbed by the QDs, as is shown in Fig. 6(d). The energy is transferred from the probe pulse to the QDs, leaving the QDs at a higher excitation state after probe pulse passage, as seen in Fig. 7(d). The probe pulse is largely absorbed over the 10–15 μm distance along the waveguide. The field emitted into the cutoff mode during passage of the probe pulse, shown in Fig. 8(d), is also significantly weaker than the probe pulse itself, consistent with assumption.

C. Pulse propagation inside all-optical logic devices

As demonstrated in Ref. [15], a weaker signal pulse E_S, acting simultaneously with E_L in the previously simulated switching system, can significantly increase the flexibility in controlling QD excitations to provide a complete set of all-optical logic operations. In this section we simulate these logic operations. In this configuration, the strong pulse E_L in the E_{L_1} channel can be viewed as the holding field, while the signal field E_S propagates in the E_{L_2} channel of the linear dispersion mode. Therefore we will denote $E_{L_1} = E_h$ and $E_{L_2} = E_S$ in this section, and replace all subscripts and superscripts of L_1 and L_2 with h and S, respectively. In all the simulation results presented below, the probe pulse is sent in (beginning of probe simulation) immediately after the holding and signal pulse simulation. The temporal separation between the peaks of the holding and signal pulses and the probe pulse is 16.5 ps.

Figures 9 and 10 show simulations of a NOT gate operation. In a logic NOT operation, the output is the opposite of the input. A NOT gate has only one input and one output. The implementation of an all-optical NOT operation in Figs. 9 and 10 includes a channel of strong, red-shifted optical holding pulses with $\Delta_{Ah} > 0$, and a simultaneous, weaker signal pulse channel ω_S nearly resonant with the right Mollow sideband of the holding pulse. The channel of optical information at carrier frequency ω_S passes through the quantum dot at the same time as the holding pulses at carrier frequency ω_h. As shown in Fig. 9, when the signal is not present (input 0), dynamic inversion results in final inverted states (excited) of the quantum dots along the waveguide [Fig. 9(c)], whereas when the signal is present (input 1), the final population becomes negative (deexcited) as shown in Fig. 10(c). The excited quantum dots will allow the passage of the subsequent probe pulse (defined as output 1) near the dot transition frequency ω_A [Fig. 9(d)], whereas the deexcited quantum dots will absorb and forbid the passage of the probe pulse (defined as output 0) [Fig. 10(d)]. As a result, an optical input of 0 in frequency channel ω_S leads to an optical output of 1 in frequency channel ω_A, and vice versa.

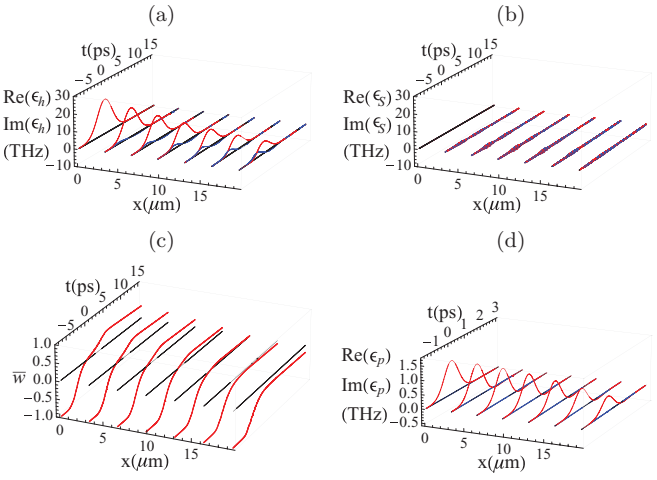

FIG. 9. (Color online) Simulated NOT gate output as 1 (probe pulse transmitted) with input of 0 (no signal pulse). $v_g = 0.24c$, $\tau = 5$ ps, $\Gamma_C = 1.88$ THz, $\Gamma_L = 4$ THz, $B = 20\ \mu\text{m}^2\,\text{ps}^{-1}$, $\gamma_{\text{high}} = 2.5$ THz, $\gamma_{\text{low}} = 5$ GHz, $\gamma_p = 0.1$ THz, $n = 10^5\ \mu\text{m}^{-3}$, $\sigma_A = 5$ THz (about 1% for QD transitions centered at 1.5 μm), $N_\sigma = 4$, $N_A = 20$, $\epsilon_h^{\max} = 20$ THz, $\epsilon_S^{\max} = 0$, $\delta\omega_C = -4$ THz, $\delta\omega_S = \omega_S - \omega_h = 23$ THz, $\overline{\Delta}_{AL} = 11$ THz, $\boldsymbol{\rho}_0 = (0,0,-1)$. (a) The holding pulse envelope function decays slowly over distance with gradual phase shift (imaginary part of the envelope function). (b) No input signal pulse envelope function, but there are minor QD radiations accumulated in the signal channel. (c) The QD average population is excited above inversion by the input holding pulse. (d) Due to the excited QD medium, a subsequent probe pulse passes through the waveguide with little attenuation.

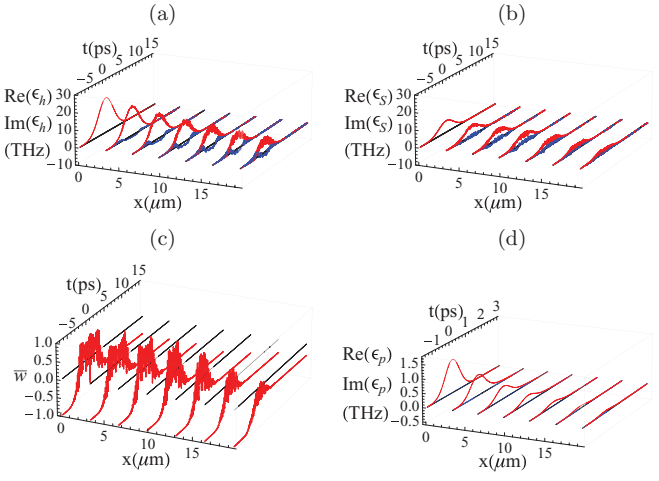

FIG. 10. (Color online) Simulated NOT gate output as 0 (probe pulse attenuated) with input of 1 (presence of a signal pulse). $\epsilon_S^{\max} = \epsilon_h^{\max}/3$, and all other parameters are the same as Fig. 9. (a) The holding pulse envelope function decays slowly over distance with gradual appearance of high frequency components and phase shift (imaginary part of the envelope function). (b) One input signal pulse envelope function gradually decays over distance with gradual appearance of high frequency components and phase shift. (c) The QD average population is deexcited by the input holding and signal pulses. (d) Due to the deexcited QD medium, a subsequent probe pulse attenuates over distance and cannot pass through the waveguide.

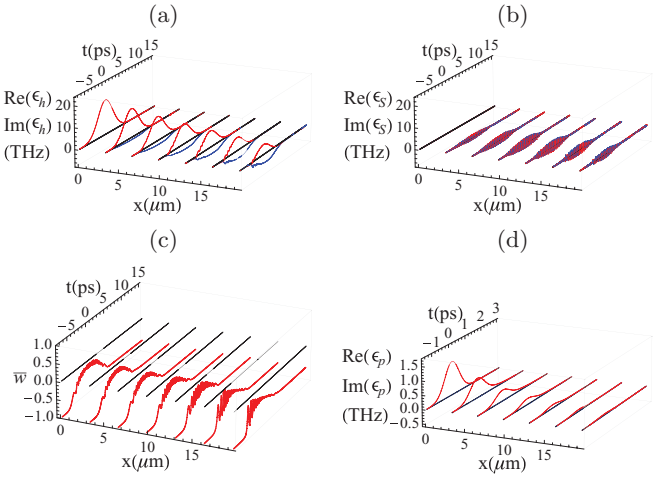

FIG. 11. (Color online) Simulated AND gate output of 0 (probe pulse attenuated) with input of (0,0) (no signal pulses). $v_g = 0.24c$, $\tau = 5$ ps, $\Gamma_C = 1.88$ THz, $\Gamma_L = 4$ THZ, $B = 20\ \mu\text{m}^2\,\text{ps}^{-1}$, $\gamma_{\text{high}} = 2.5$ THz, $\gamma_{\text{low}} = 5$ GHz, $\gamma_p = 0.1$ THz, $n = 10^5\ \mu\text{m}^{-3}$, $\sigma_A = 5$ THz (about 1% for QD transitions centered at 1.5 μm), $N_\sigma = 4$, $N_A = 20$, $\epsilon_h^{\max} = 16$ THz, $\epsilon_S^{\max} = 0 \times 2.26 = 0$ THz, $\delta\omega_C = -13.5$ THz, $\delta\omega_S = \omega_S - \omega_h = -12.5$ THz, $\overline{\Delta}_{AL} = -6$ THz, $\boldsymbol{\rho}_0 = (0,0,-1)$. (a) The holding pulse envelope function decays slowly over distance with gradual phase shift (imaginary part of the envelope function). (b) No input signal pulse envelope function, but there are significant QD radiations accumulated in the signal channel. (c) The QD average population is deexcited by the input holding pulse. (d) Due to the deexcited QD medium, a subsequent probe pulse attenuates over distance and cannot pass through the waveguide.

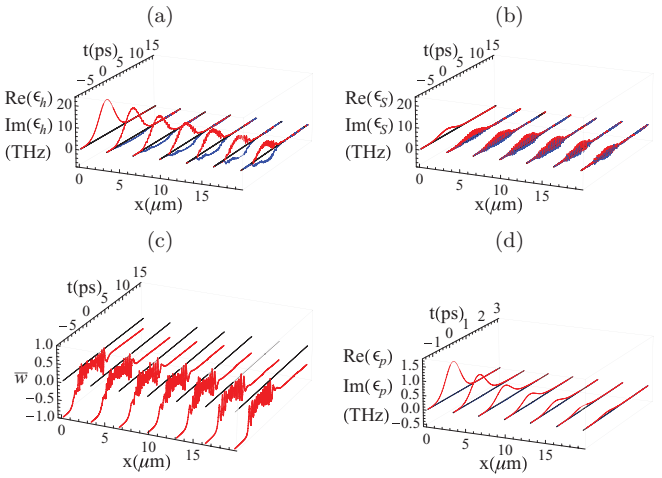

FIG. 12. (Color online) Simulated AND gate output of 0 (probe pulse attenuated) with input of (0,1) (one signal pulse). $\epsilon_S^{\max} = 2.26$ THz, and all other parameters are the same as Fig. 11. (a) The holding pulse envelope function decays slowly over distance with gradual appearance of high frequency components and phase shift. (b) One input signal pulse envelope function propagates with gradual appearance of significant high frequency components. (c) The QD average population is deexcited by the input holding and signal pulses. (d) Due to the deexcited QD medium, a subsequent probe pulse attenuates over distance and cannot pass through the waveguide.

A reasonable switching contrast of the probe pulse is reached at a waveguide length scale 10 μm. The factors determining this length scale will be further discussed in Sec. III E. Below this length scale, the deexcited quantum dots do not have enough distance to absorb the probe pulse in Fig. 10(d). Above this length scale, the holding pulse does not have enough power to invert the quantum dots [apparent from attenuation of the holding pulse in Fig. 9(a) and deterioration of inversion level in Fig. 9(c) as pulse travel distance increases]. Accordingly, the probe pulse amplitude starts to decrease over distance [Fig. 9(d)]. Also, the holding and signal pulses gradually pick up higher frequency components (Fig. 10) over distance, accompanied with imaginary components of the pulse envelop functions. However, the pulse shapes are generally preserved within the 10 μm length scale.

Figures 11 to 13 and Figs. 14 to 16 demonstrate all-optical AND gate and OR gate operations, respectively. In a logic AND operation, the output is positive only if both of the two inputs are positive, whereas a logic OR operation results in the output being positive if either of the two inputs is positive. These two logic operations can be realized with two streams of optical information at frequency ω_S passing through the quantum dots at the same time as the strong holding pulse at ω_h with $\Delta_{Ah} < 0$. The signal pulse frequency ω_S is near resonant with the left Mollow side band of the holding pulse [15]. Depending on the relative strengths of the holding and signal pulses, the proposed device can perform either logic AND or OR operations.

For a relatively large ϵ_h, the final inversion increases monotonically with ϵ_s. This can be utilized to perform logic AND operations, where only the addition of two signal pulses [input (1,1)] is strong enough to switch the population to positive inversion [Fig. 13(c)], while inputs of (0,0) [Fig. 11(c)] and (0,1) [Fig. 12(c)] all result in final populations below inversion. As a result, a subsequent probe pulse ϵ_p can only pass through the waveguide after input signals of (1,1) [Fig. 13(d)], but will be attenuated after inputs of (0,0) and (0,1) [Figs. 11(d) and 12(d), respectively].

On the other hand, for a relatively small ϵ_h, the final inversion easily reaches saturation with increasing ϵ_S. This can be utilized to perform logic OR operations, where the presence of both or either signal(s) [input (1,1) or (0,1)] are enough to switch the population to positive inversion [Figs. 16(c) and 15(c)], while inputs of (0,0) [Fig. 14(c)] results in final populations below inversion. As a result, a subsequent probe pulse ϵ_p can pass through the waveguide after input signals of either (1,1) [Fig. 16(d)] or (0,1) [Fig. 15(d)], but will be attenuated after inputs of (0,0) [Fig. 14(d)].

Similar to the NOT gate, a satisfactory transmission contrast of the probe pulse can be realized on the 10 μm length scale for the AND and OR gates. The holding pulses and signal pulses also pick up high frequency and imaginary components as they travel along the waveguide. The phase shift (appearance of imaginary part for the pulse envelope functions) is not very pronounced after propagating for 10 μm, since it remain well below $\pi/4$ (imaginary part much less than the real part) in most cases. The high frequency components, on the other hand, require much more attention. A comparison from Fig. 9 to Fig. 16 implies that the high frequency components may arise from crosstalk between the holding pulse channel and the signal pulse channel, due to their coupling to the common QD polarization field. The accumulation of high frequency

components in one channel depends on the presence of pulses in the other channel. It always occurs in the signal channel (holding pulse is always present), whereas it only occurs in the holding pulse channel when the input signal is not 0. Since the holding pulse is always much stronger than the signal pulses, the high frequency components remain less than an order of magnitudes weaker than the holding pulse itself after propagating for 10 μm. However, high frequency noise can be much more significant in the signal channel, sometimes entirely distorting the input signal [Figs. 11(b) to 15(b)]. This may require correction in a practical device design.

D. Probe pulse soliton formation

We have shown that a resonant probe pulse will pass through the waveguide without attenuation, following the QD excitation by a red-shifted control pulse in our all-optical switch [Fig. 6(c)]. Here we consider the further evolution of the probe pulse over distances much longer than the proposed 10 μm device length.

Provided the probe pulse is not strong enough to push the Mollow sidebands into the high LDOS region, pulse transmission and reshaping is equivalent to that of an amplifying medium in ordinary vacuum [27,28]. In this case [28], if the probe pulse continues propagating along the active QD medium inside the waveguide, then it is possible for the pulse to evolve into a stable π pulse soliton. This assumes the presence of a broadband background linear loss for the waveguide linear

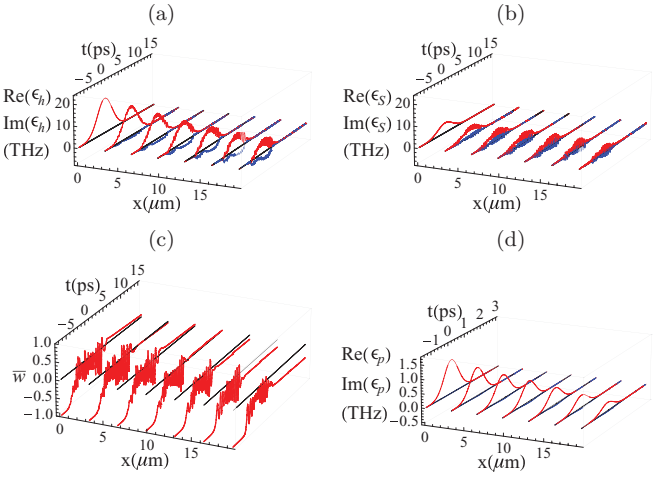

FIG. 13. (Color online) Simulated AND gate output of 1 (probe pulse transmitted) with input of (1,1) (two signal pulses). $\epsilon_S^{\max} = 2 \times 2.26\,\text{THz} = 4.52\,\text{THz}$, and all other parameters are the same as Fig. 11. (a) The holding pulse envelope function decays slowly over distance with gradual appearance of high frequency components and phase shift. (b) Two input signal pulse envelope functions (added together) propagate with gradual appearance of significant high frequency components. (c) The QD average population get excited barely above inversion by the input holding and signal pulses. (d) Due to the barely excited QD medium, a subsequent probe pulse pass through the waveguide with some attenuation. The probe pulse output contrast between the on and off [Figs. 11(d) and 12(d)] states is not as good as that for the NOT gate, but still distinguishable. This is due to the low inversion level achieved here.

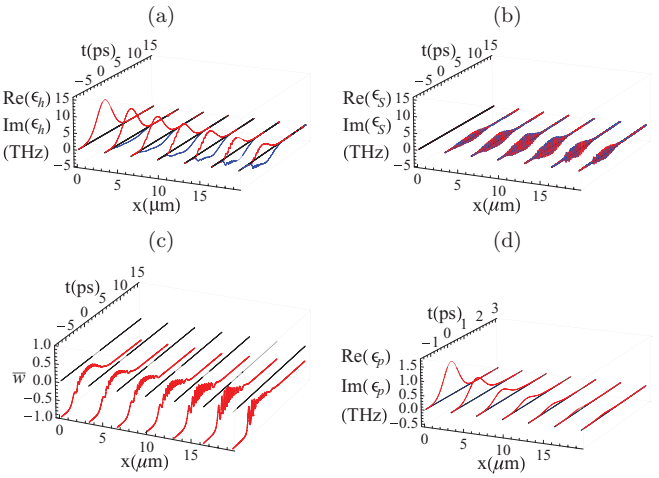

FIG. 14. (Color online) Simulated OR gate output of 0 (probe pulse attenuated) with input of (0,0) (no signal pulses). $v_g = 0.24c$, $\tau = 5$ ps, $\Gamma_C = 1.88$ THz, $\Gamma_L = 4$ THz, $B = 20\,\mu\text{m}^2\,\text{ps}^{-1}$, $\gamma_{\text{high}} = 2.5$ THz, $\gamma_{\text{low}} = 5$ GHz, $\gamma_p = 0.1$ THz, $n = 10^5\,\mu\text{m}^{-3}$, $\sigma_A = 5$ THz (about 1% for QD transitions centered at 1.5 μm), $N_\sigma = 4$, $N_A = 20$, $\epsilon_h^{\max} = 10.5$ THz, $\epsilon_S^{\max} = 0 \times 2.26\,\text{THz} = 0$ $\delta\omega_C = -13.5$ THz, $\delta\omega_S = \omega_S - \omega_h = -12.5$ THz, $\overline{\Delta}_{AL} = -6$ THz, $\boldsymbol{\rho}_0 = (0,0,-1)$. (a) The holding pulse envelope function decays slowly over distance with gradual phase shift. (b) No input signal pulse envelope function, but there is significant QD radiation accumulated in the signal channel. (c) The QD average population is deexcited by the input holding pulse. (d) Due to the deexcited QD medium, a subsequent probe pulse attenuates over distance and cannot pass through the waveguide.

dispersion mode. We confirm this soliton formation through the numerical simulation of our Maxwell-Bloch equations.

Figure 17(a) shows the formation of a probe pulse soliton, assuming a uniformly excited QD medium with $\overline{w}(0) = 0.2$ (in practice it is difficult to obtain uniform excitation over such an extended distance). All parameters are kept the same as Fig. 6. The probe pulse is reshaped gradually into a π pulse soliton [the soliton area is confirmed by the fact that w reverses sign in a half circle of the Bloch vector rotation without additional oscillations, as shown in Fig. 17(b)] after propagating approximately 300 μm inside the active QD medium. It then continues propagation without distortion. Slight loss of energy is observed after the soliton formation, due to the small radiative decay rate $\gamma_{\text{low}} = 5$ GHz in the low LDOS region. This is not due to the background linear loss rate Γ_L. This simulation demonstrates that the typical (10 μm) length of our proposed switching device is insufficient for stable soliton formation.

E. Discussion

Our simulation parameters are estimated based on the 15 unit cell 2D-3D PBG heterostructure waveguide in Ref. [16]. The length of the active region is about 9 μm for light at 1.5 μm, with a 600 nm unit cell length [16]. Our simulation results demonstrate that satisfactory picosecond probe pulse switching and logic operation contrasts are achieved within this length scale, over which the control and holding pulses and signal pulses do not suffer significant distortion. Our study

demonstrates that picosecond all-optical switching and all-optical logic is theoretically achievable on a 10 μm length scale in a PBG waveguide through Bloch dynamics of embedded quantum dots.

According to Eqs. (9), (12), (24), and (25), several input parameters determine the required active waveguide length $x_{\text{waveguide}}$ to produce satisfactory optical switching contrasts of the probe pulse. The most important are those characterizing the embedded QD medium. Increasing the quantum dot number density n and using QDs with larger dipole μ would increase the radiation source terms of both envelop equations, enhancing their radiative reaction for pulse reshaping. Furthermore, larger dipole per dot leads to stronger QD-field coupling (larger Rabi frequencies for given field strength), enabling larger QD population switching contrast [13,14]. These effects lead to shorter device length for producing the required optical switching and logic contrast.

Another important factor influencing output contrast is the host photonic-crystal waveguide geometry, and the resulting dispersion curves. For the linear dispersion mode, a lower group velocity v_g spatially compresses the pulse, leading to larger peak field strength with a given amount of energy per pulse. This enables larger QD population switching contrast (slow light enhancement of nonlinear effect). This should more than compensate the reduction in the source term in Eq. (24) caused by smaller group velocity. For the cutoff mode (responsible for providing the density of state discontinuity), achieving a larger LDOS within a limited waveguide length is critical for maximizing QD population switching contrast.

From the above discussion, the required active waveguide length scale is inversely proportional to the polarization enhancement effect of n and μ [$L_{\text{waveguide}} \propto 1/(n\mu)$]. However, the dependence of $L_{\text{waveguide}}$ on the QD population switching

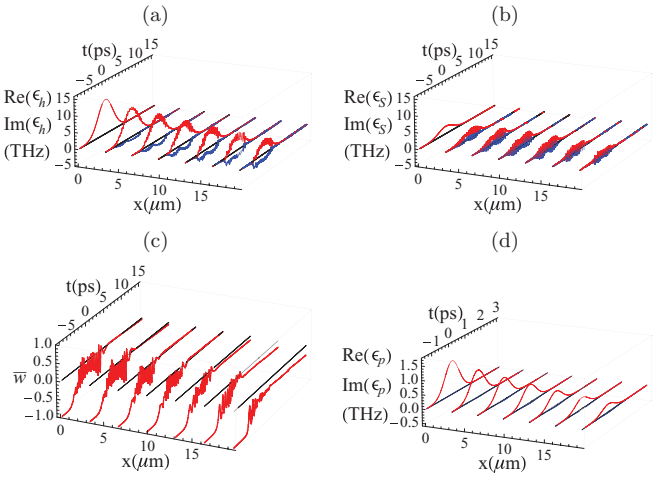

FIG. 15. (Color online) Simulated OR gate output of 1 (probe pulse transmitted) with input of (0,1) (one signal pulse). $\epsilon_S^{\max} = 2.26$ THz, and all other parameters are the same as Fig. 14. (a) The holding pulse envelope function decays slowly over distance with gradual phase shift and high frequency components. (c) The QD average population is excited barely above inversion by the input holding and signal pulses. (d) Due to the barely excited QD medium, a subsequent probe pulse passes through the waveguide with some attenuation.

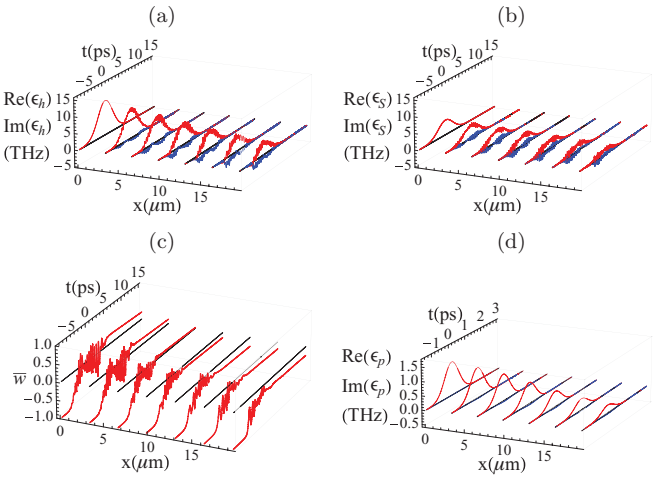

FIG. 16. (Color online) Simulated OR gate output of 1 (probe pulse transmitted) with input of (1,1) (two signal pulses). $\epsilon_S^{\max} = 2 \times 2.26$ THz $= 4.52$ THz, and all other parameters are the same as Fig. 14. (a) The holding pulse envelope function decays slowly over distance with gradual appearance of high frequency components and phase shift. (b) Two input signal pulse envelope functions (added together) propagate with gradual appearance of significant high frequency components. (c) The QD average population is excited barely above inversion by the input holding and signal pulses. (d) Due to the barely excited QD medium, a subsequent probe pulse passes through the waveguide with some attenuation. The probe pulse output contrast between the on and off [Fig. 11(d)] states is not as good as that for the NOT gate, but still distinguishable. This is due to the low inversion level achieved here.

contrast enhancement effects from μ, v_g, and γ_-/γ_+ is harder to quantify through simple analytical expressions, due to the highly nonlinear nature of the switching mechanism. In general a shorter active waveguide length is sufficient with larger dipole μ, smaller group velocity v_g, and larger LDOS jump contrast γ_-/γ_+.

The energy per pulse for all-optical switching applications has been estimated to be as little as 1.6 fJ under specific assumptions of the waveguide cross-sectional geometry, field distribution, and group velocity [14]. However, the required active waveguide length scale as discussed above is independent of the cross-section areas in our model. Although a larger

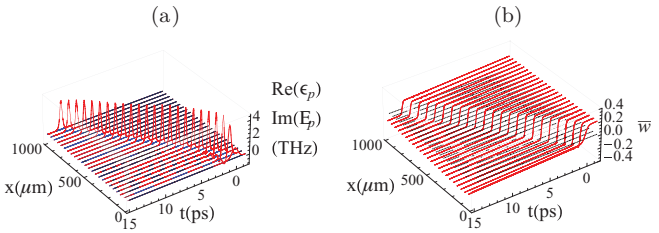

FIG. 17. (Color online) Evolution of the probe pulse into a π pulse soliton when propagating long enough inside the active QD medium already excited by the red-shifted control pulse. The initial population is set to $\overline{w}(0) = 0.2$, and all other parameters are the same as Fig. 6. (a) Evolution of the pulse envelope function. The input pulse starts at $x = 0$ with area π, and gets reshaped over distance until reaching a stable shape and group velocity, at around $x = 300$ μm. (b) Evolution of the QD average population.

cross-section area could mean more QDs being embedded with a given number density n, it also leads to scaled increase in energies per pulse to be absorbed by the active QDs. Under our uniform field and QD distribution assumption in the cross-sectional direction, it is the QD number density n, instead of the absolute number of QDs, that enters our envelope equations governing the pulse propagation. However, in reality the actual cross-sectional field and QD distribution, as well as the overlap between the two, is a critical issue to be addressed when designing practical waveguide structures for all-optical information processing applications.

IV. CONCLUSION

In summary, we have developed a coupled Maxwell-Bloch theory in the slowly varying envelope approximation for simulation of optical pulse propagation inside ultrafast all-optical switching and logic devices. This is based on a bimodal PC waveguide embedded with two-level QDs. Instead of full simulation of Maxwell's equation involving microscopic details of PBG waveguide architecture in 3D, we abstract the key properties of the waveguide to simplify the electromagnetic modeling. Using mode parameters extracted from a realistic 2D-3D PBG heterostructure waveguide [16], we have demonstrated picosecond all-optical switching and logic devices on a 10 μ m length scale. The switching contrasts generally deteriorates with increasing inhomogeneous broadening, but is still satisfactory at the 1% level (for QD transitions centered at 1.5 μm) as shown in our simulation results.

The switching contrast of the QD populations (and hence the probe pulse contrast) could be further improved if we take into account stimulated emission and coherent feedback effects coming from a finite band of radiation into the cutoff mode [19]. This effect is not captured in our model because the envelop equation of the cutoff mode [Eq. (25)] only describes a very narrow frequency range in the immediate vicinity of the cutoff frequency. The full FDTD simulation of Ref. [19] demonstrates remarkable high-contrast QD population switching with relatively modest (factor of 10) jump discontinuities in the electromagnetic LDOS. Non-Markovian radiative feedback effects of this nature could enable subpicosecond switching and logic to be realized even in 2D photonic-crystal waveguides or in active waveguide segments less than 10 μm in length.

A more detailed microscopic understanding of dephasing and nonradiative decay of excited quantum dots may be required to determine the minimum time scale between logic operations. Such damping effects are needed to erase memory of a previous logic operation prior to a new one being performed.

ACKNOWLEDGMENTS

This work was supported in part by the Natural Sciences and Engineering Research Council of Canada and the Canadian Institute for Advanced Research.

APPENDIX A: ENVELOPE EQUATION OF THE LINEAR DISPERSION MODE

The waveguide mode for the input laser pulse has approximately linear dispersion. This dispersion can be characterized by the group velocity v_g at which the pulse envelope $\tilde{E}_{L_1,L_2}(x,t)$ travels, and the phase velocity $\omega_{L_1,L_2}/k_{L_1,L_2}$ at which the carrier optical phase $e^{-i(\omega_{L_1,L_2}t-k_{L_1,L_2}x)}$ imposed on $\tilde{E}_{L_1,L_2}(x,t)$ travels. We model the movement of the envelope function $\tilde{E}_{L_1,L_2}(x,t)$ through an effective homogeneous medium whose dielectric constant ε is defined through the group velocity (slope of the dispersion curve):

$$v_g = c/\sqrt{\varepsilon}. \tag{A1}$$

An electromagnetic pulse propagating through this effective medium will have the following form:

$$E_{\text{eff}} = \tilde{E}_{L_1,L_2} e^{-i[\omega_{L_1,L_2}t-(\omega_{L_1,L_2}/v_g)x]}. \tag{A2}$$

Accordingly the polarization takes the form

$$P_{\text{eff}} = \mu n\left(\langle\tilde{\sigma}_{12}^{L_1,L_2}\rangle e^{-i[\omega_{L_1,L_2}t-(\omega_{L_1,L_2}/v_g)x]} + \text{c.c.}\right). \tag{A3}$$

E_{eff} obeys the following Maxwell's equation:

$$\frac{\partial^2 E_{\text{eff}}}{\partial x^2} - \frac{\varepsilon}{c^2}\frac{\partial^2 E_{\text{eff}}}{\partial t^2} = \frac{4\pi}{c^2}\frac{\partial^2 P_{\text{eff}}}{\partial t^2}. \tag{A4}$$

To simplify notations, in the following, we use subscript L to denote both subscript L_1 and L_2 for the first and second linear dispersion mode. To derive the envelope equation for $\tilde{E}(x,t)$, we assume $\tilde{E}(x,t)$ is slowly varying both temporally on the ω_L^{-1} time scale and spatially on the $\max(\omega_L/v_g,k_L)^{-1}$ length scale. Under these assumptions, substituting Eqs. (A1), (A2), and (A3) into Eq. (A4), and by making the slowly varying envelope approximations, we obtain the following envelope equation:

$$\frac{\partial\tilde{E}_L}{\partial x} + \frac{1}{v_g}\frac{\partial\tilde{E}_L}{\partial t} = \frac{2i\pi\mu n\omega_L v_g}{c^2}\langle\tilde{\sigma}_{12}^{L}\rangle. \tag{A5}$$

Furthermore, we use a linear broad band loss rate Γ_L to describe either additional absorption losses or decay of the optical mode from a finite segment of the PBG waveguide. By including this linear loss term into the envelope Eq. (A5) we obtain Eq. (18).

APPENDIX B: POLARIZATION ENVELOP IN THE FRAME OF THE CUTOFF MODE

In deriving the equation of motion for $\tilde{E}_C(x,t)$, we write P in a way different from Eq. (15):

$$\begin{aligned} P(x,t) &= \mu n(\langle\sigma_{12}\rangle_{\text{avg}} + \text{c.c.}) \\ &= \mu n\left[\langle\tilde{\sigma}_{12}^{C}\rangle(e^{-i(\omega_C t-k_c x)} + e^{-i(\omega_C t+k_C x)}) + \text{ c.c.}\right]. \end{aligned} \tag{B1}$$

Now $\langle\tilde{\sigma}_{12}^{C}\rangle$ is the envelope function of the average QD dipole expectation value $\langle\sigma_{12}\rangle_{\text{avg}}$ in the frame of the cutoff mode $e^{-i(\omega_C t-k_c x)} + e^{-i(\omega_C t+k_C x)}$. As is the case for $\langle\tilde{\sigma}_{12}^{L_1}\rangle$, $\langle\tilde{\sigma}_{12}^{C}\rangle$ also encompasses all the frequency components of the QD dipole.

From Eqs. (15) and (B1) we have

$$\mathrm{Re}\left[\langle\tilde{\sigma}_{12}^{C}\rangle\left(e^{-i(\omega_C t-k_c x)}+e^{-i(\omega_C t+k_C x)}\right)\right]=\mathrm{Re}\left(\langle\tilde{\sigma}_{12}^{L_1}\rangle e^{-i(\omega_{L_1}t-k_{L_1}x)}\right). \tag{B2}$$

For physical problems, the imaginary parts of $\langle\tilde{\sigma}_{12}^{C}\rangle(e^{-i(\omega_C t-k_c x)}+e^{-i(\omega_C t+k_C x)})$ and $\langle\tilde{\sigma}_{12}^{L_1}\rangle e^{-i(\omega_{L_1}t-k_{L_1}x)}$ are irrelevant, because they are canceled out by their complex conjugates and do not contribute to the polarization function. This gives us the freedom to impose a condition:

$$\mathrm{Im}\left[\langle\tilde{\sigma}_{12}^{C}\rangle\left(e^{-i(\omega_C t-k_c x)}+e^{-i(\omega_C t+k_C x)}\right)\right]=\mathrm{Im}\left(\langle\tilde{\sigma}_{12}^{L_1}\rangle e^{-i(\omega_{L_1}t-k_{L_1}x)}\right). \tag{B3}$$

Equations (16), (B2), and (B3) together imply Eq. (23).

[1] S. John, Phys. Rev. Lett. **53**, 2169 (1984).
[2] S. John, Phys. Rev. Lett. **58**, 2486 (1987).
[3] V. P. Bykov, Sov. J. Quantum Electron. **4**, 861 (1975).
[4] E. Yablonovitch, Phys. Rev. Lett. **58**, 2059 (1987).
[5] A. Chutinan, S. John, and O. Toader, Phys. Rev. Lett. **90**, 123901 (2003).
[6] A. Chutinan and S. John, Phys. Rev. E **71**, 026605 (2005).
[7] A. Chutinan and S. John, Phys. Rev. B **72**, 161316 (2005).
[8] A. Chutinan and S. John, Opt. Express **14**, 1266 (2006).
[9] T. Y. M. Chan and S. John, Phys. Rev. A **78**, 033812 (2008).
[10] M. Florescu and S. John, Phys. Rev. A **69**, 053810 (2004).
[11] M. Florescu and S. John, Phys. Rev. A **64**, 033801 (2001).
[12] S. John and M. Florescu, J. Opt. A: Pure Appl. Opt. **3**, S103 (2001).
[13] X. Ma and S. John, Phys. Rev. Lett. **103**, 233601 (2009).
[14] X. Ma and S. John, Phys. Rev. A **80**, 063810 (2009).
[15] X. Ma and S. John, Phys. Rev. A **84**, 013830 (2011).
[16] R. Wang and S. John, Phys. Rev. A **70**, 043805 (2004).
[17] D. Vujic and S. John, Phys. Rev. A **76**, 063814 (2007).
[18] D. Vujic and S. John, Phys. Rev. A **79**, 053836 (2009).
[19] H. Takeda and S. John, Phys. Rev. A **83**, 053811 (2011).
[20] R. W. Boyd, *Nonlinear Optics*, 2nd ed. (Academic, New York, 2003).
[21] N. Akozbek and S. John, Phys. Rev. E **57**, 2287 (1998).
[22] N. Akozbek and S. John, Phys. Rev. E **58**, 3876 (1998).
[23] L. C. Andreani, G. Panzarini, and J. M. Gerard, Phys. Rev. B **60**, 13276 (1999).
[24] T. H. Stievater, X. Li, D. G. Steel, D. Gammon, D. S. Katzer, D. Park, C. Piermarocchi, and L. J. Sham, Phys. Rev. Lett. **87**, 133603 (2001).
[25] J. P. Reithmaier, G. Sek, A. Loffler, C. Hofmann, S. Kuhn, S. Reitzenstein, L. V. Keldysh, V. D. Kulakovskii, T. L. Reinecke, and A. Forchel, Nature (London) **432**, 197 (2004).
[26] G. Sewell, *The Numerical Solution of Ordinary and Partial Differential Equations*, 2nd ed. (John Wiley, New York 2005).
[27] L. Allen and J. H. Eberly, *Optical Resonance and Two-level Atoms* (John Wiley, New York, 1975).
[28] V. S. Letokhov, Sov. Phys. JETP **29**, 221 (1969).